Article

Optimization of Active Current for Large-Scale Wind Turbines Integrated into Weak Grids for Power System Transient Stability Improvement

Dongliang Zhang [iD] **and Xiaoming Yuan** *

State Key Laboratory of Advanced Electromagnetic Engineering Technology,
Huazhong University of Science and Technology, Wuhan 430074, China; zhangdl@hust.edu.cn
* Correspondance: yuanxm@hust.edu.cn; Tel.: +86-27-8754-4359

Abstract: Power system transient stability is a challenge when integrating large-scale wind turbines into weak grids. This paper addresses the issue of transient stability in such situations by optimizing a wind turbine's active current behavior. A wind turbine's active current reference controller and its setting optimization method are proposed based on analyses of two associated problems: the mechanism for improving transient stability of a single (synchronous) machine infinite bus (SMIB) system, as well as the various physical factor dependencies dictating how active and reactive wind turbine currents affect the swing dynamics of synchronous machines. Analysis of the first problem guided the design of the controller's main structure. Analysis of the second problem guided selection of the control object within a wind turbine's active and reactive currents, as well as helped recognition of the influential physical factors that must be considered in the parameter setting process. The efficiency of the controller and the validity of the analyses were verified by case studies using Kundur's two-area system.

Keywords: power system; transient stability; weak grid; wind turbine

1. Introduction

Wind turbines are being increasingly integrated into weak grids that possess limited synchronous generators (i.e., are inertia weak) or long transmission lines (i.e., are link weak), a situation found in many areas in China [1]. The impact of this large-scale integration of wind turbines on power system stability in such systems has been widely studied in terms of transient stability [2–5], small signal stability [6,7], and frequency stability [8]. Based on these studies, many optimizations or re-designs of wind turbine controllers have been proposed to improve different aspects of power system stability [9–16].

In terms of transient stability, Ullah et al. [11] proposed an E.ON-grid-code-compliant current reference controller that preferentially boosted the reactive current in proportion to the voltage dip to simultaneously support the system voltage and improve transient stability. A study by Weise [12] further revealed there was a beneficial effect of the accompanied active current reduction with this type of controller on transient stability, and discussed the optimum setting of the proportional gain for reactive current boosting. Furthermore, [13] proposed an independent active current reduction controller that optimized the active current reference with a multiplier approximately proportional to the square of the remaining voltage. In addition, [14] proposed a torque reference controller that optimized the torque reference based on the terminal frequency for a rigid interval subsequent to a fault. Reference [15] proposed a swing-equation-based constant-virtual-inertia control of wind turbines (virtual synchronous generators), and suggested a large constant virtual inertia setting for

transient stability improvement. Comparatively, Alipoor et al. [16] proposed a mutative virtual inertia controller, wherein each swing cycle of the virtual synchronous generator was divided into four stages, and the virtual inertia was set to be large for stages 1 and 3 and small for stages 2 and 4. A considerable improvement in transient stability was reported in the study.

Although numerous controllers have been proposed, and many associated problems have also been analyzed in the studies reviewed above, there are still two issues that have not received much attention. The first problem is the mechanism underlying transient stability improvement within a single (synchronous) machine infinite bus (SMIB) system. An analysis of this mechanism for simple SMIB systems can produce engineering insights that can be used to guide the design of the main structure of a controller for transient stability improvement in systems that are more complex. Another problem is how the capability of the active and reactive currents of a wind turbine are dependent on various physical factors—such as the location of the wind turbines and the strength of the grid—in terms of affecting the swing dynamics of synchronous machines. An analysis of the dependencies for simple systems can produce engineering insights that can be used to guide selection of the control object within a wind turbine's active current and reactive current, as well as help recognition of the influential physical factors that must be considered in the parameter setting process for complex systems.

This paper first analyzes these two associated problems for very simple systems. The engineering insights gained are then used to design a wind turbine active current reference controller and its settings optimization in order to improve power system transient stability when large-scale wind turbines are integrated into weak grids. Finally, the paper will present an application of the proposed controller and its setting approach using Kundur's two-area system modified by wind turbine integration.

The rest of this paper is organized as follows. Sections 2 and 3 present analyses of the two problems, respectively. Section 4 introduces the proposed controller and its settings approach. Section 5 provides the case study using Kundur's two-area system, while Section 6 concludes the paper.

2. Analysis of the Mechanism for Transient Stability Improvement in Single Machine Infinite Bus (SMIB) Systems

Using the stage division criterion developed by Alipoor et al. [16], we reevaluate the mechanism providing transient stability improvement in an SMIB system. As illustrated in Figure 1b, Alipoor et al. divided each swing cycle of the SMIB system shown in Figure 1a into four stages. The interval with a positive rotor acceleration and a positive rotor speed deviation from its post-fault stable equivalent point (SEP) (assumed to be 1 p.u.) is stage 1; the interval with a negative rotor acceleration and a positive rotor speed deviation is stage 2, the interval with negative acceleration and negative speed deviation is stage 3, and the interval with positive acceleration and negative speed deviation is stage 4.
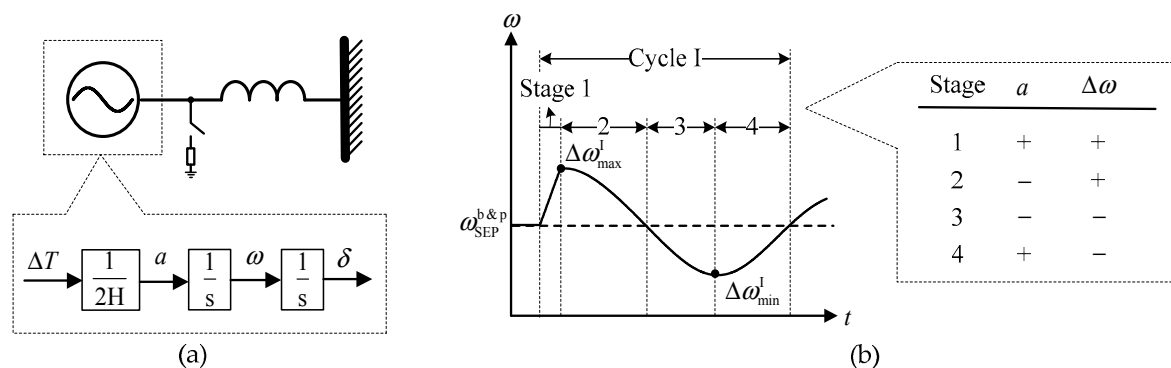

Figure 1. Schematic diagram of (**a**) the single machine infinite bus (SMIB) system and (**b**) the four-stage division criterion.

2.1. Quantitative Relationship between the Motivating Equivalent Rotor Acceleration of Each Stage and the Resulting Extrema of Rotor Speed and Angle Deviation from the Respective Post-Fault SEP Value

The transient stability of a SMIB system is, in fact, the stability of two variables, the rotor speed and rotor angle; both are essentially motivated by the rotor acceleration, as Figure 1a exhibits. By using a constant rotor acceleration that equals the true time-varying acceleration in each stage, the quantitative relationship between rotor acceleration, rotor speed deviation, and rotor angle deviation during each stage can be written as

$$|\Delta\omega| = \Delta t \times |a|; \ |\Delta\delta| = (\Delta t \times |\Delta\omega|)/2 \tag{1}$$

Figure 2 illustrates the typical swing process of a SMIB system, where the synchronous machine is accelerating during a fault and its rotor angle has passed the post-fault SEP value at fault clearance. The rotor acceleration is deliberately set to be constant during each stage, respectively denoted as a_1^{I}, a_2^{I}, a_3^{I} ...
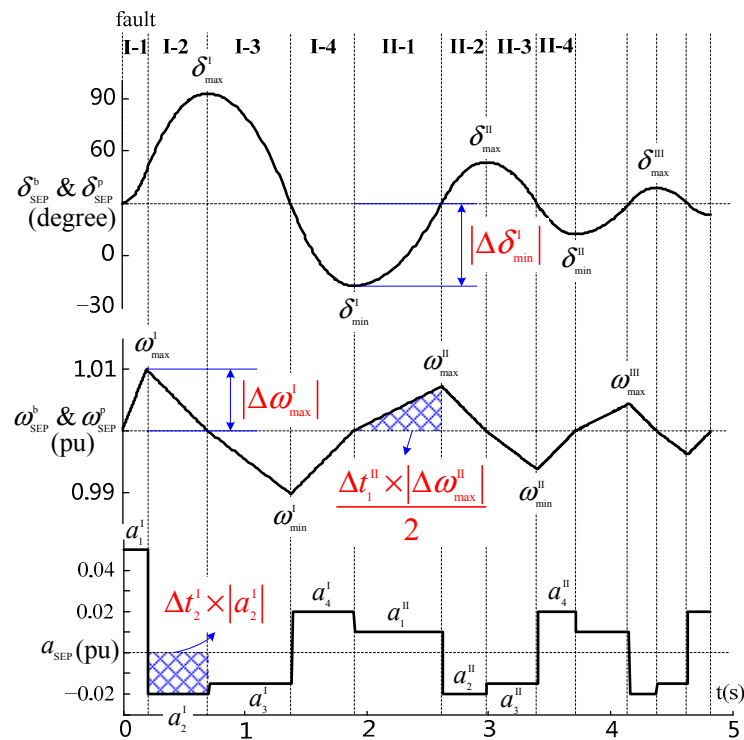

Figure 2. A typical swing process in a SMIB system. The pre- and post-fault SEP rotor angle is 30 degrees. Rotor acceleration during fault is 0.05 p.u. and lasts for 200 ms; rotor acceleration post fault is 0.01 p.u. in stage 1, -0.02 p.u. in stage 2, -0.015 p.u. in stage 3, and 0.02 p.u. in stage 4.

By repeatedly applying (1), the quantitative relationships between the motivating accelerations and the resulting extrema in speed and angle deviations for different swing processes of the SMIB system can be obtained. The expressions are slightly different depending on whether the synchronous machine is accelerating or decelerating during fault and whether or not the rotor angle has passed its post-fault SEP value at fault clearance; the expressions are presented in a dense form as follows.

The extrema of the deviations in rotor angle and speed from their respective SEP value in the first cycle, reflecting the first and second swing stabilities, are given by

$$\left|\Delta\delta^{\mathrm{I}}_{\max,\min}\right| = \begin{cases} \frac{1}{2}\left|a^{\mathrm{I}}_{1,3}\right|\left(1 + \frac{\left|a^{\mathrm{I}}_{1,3}\right|}{\left|a^{\mathrm{I}}_{2,4}\right|}\right)t^2_{\mathrm{clr}} - \left|\Delta\delta_{\mathrm{SEP}}\right|, & \text{Passed} \\[2mm] \frac{\left|a^{\mathrm{I}}_{1,3}\right|}{\left|a^{\mathrm{I}}_{2,4}\right|}\left|\Delta\delta_{\mathrm{SEP}}\right|, & \text{Not passed} \end{cases} \tag{2}$$

$$\left|\Delta\delta^{\mathrm{I}}_{\min,\max}\right| = \frac{\left|a^{\mathrm{I}}_{3,1}\right|}{\left|a^{\mathrm{I}}_{4,2}\right|}\left|\Delta\delta^{\mathrm{I}}_{\max,\min}\right| \tag{3}$$

$$\left|\Delta\omega^{\mathrm{I}}_{\max,\min}\right| = \begin{cases} \left|a^{\mathrm{I}}_{1,3}\right|t_{\mathrm{clr}}, & \text{Passed} \\[2mm] \sqrt{2\left|a^{\mathrm{I}}_{1,3}\right|\left|\Delta\delta_{\mathrm{SEP}}\right|}, & \text{Not passed} \end{cases} \tag{4}$$

$$\left|\Delta\omega^{\mathrm{I}}_{\min,\max}\right| = \sqrt{2\left|a^{\mathrm{I}}_{3,1}\right|\left|\Delta\delta^{\mathrm{I}}_{\max,\min}\right|} \tag{5}$$

where the ",," in subscript means "or", with the former representing the situation when the synchronous machine accelerates during fault and the latter decelerates, the Arabic numerals in subscript are the stage number, the Roman numerals in superscript are the cycle number, the "clr" in subscript means fault clearance, the "Passed" in (2) and (4) represents the situation when the rotor angle has passed the post-fault SEP value at fault clearance and the "Not passed" represents the situation when the rotor angle has not passed. Furthermore,

$$\Delta\delta_{\mathrm{SEP}} \triangleq \delta^{\mathrm{p}}_{\mathrm{SEP}} - \delta^{\mathrm{b}}_{\mathrm{SEP}} \tag{6}$$

$$\Delta\delta_{\max,\min} \triangleq \text{maximum or minimum of } \left(\delta - \delta^{\mathrm{p}}_{\mathrm{SEP}}\right) \tag{7}$$

$$\Delta\omega_{\max,\min} \triangleq \text{maximum or minimum of } \left(\omega - \omega^{\mathrm{p}}_{\mathrm{SEP}}\right) \tag{8}$$

where the superscript "p" represents "post fault", and "b" represents "before fault".

The extrema and their decays in subsequent cycles reflect aperiodic and oscillatory stabilities after the first cycle, and can be deduced as follows

$$\frac{\left|\Delta\delta^{\mathrm{N+I}}_{\max}\right|}{\left|\Delta\delta^{\mathrm{N}}_{\max}\right|} = \frac{\left|\Delta\delta^{\mathrm{N+I}}_{\min}\right|}{\left|\Delta\delta^{\mathrm{N}}_{\min}\right|} = \frac{|a_1||a_3|}{|a_2||a_4|} \quad \mathrm{N} = \mathrm{I, II,} \dots \tag{9}$$

$$\frac{\left|\Delta\omega^{\mathrm{N+I}}_{\max}\right|}{\left|\Delta\omega^{\mathrm{N}}_{\max}\right|} = \frac{\left|\Delta\omega^{\mathrm{N+I}}_{\min}\right|}{\left|\Delta\omega^{\mathrm{N}}_{\min}\right|} = \sqrt{\frac{|a_1||a_3|}{|a_2||a_4|}} \quad \mathrm{N} = \mathrm{I, II,} \dots \tag{10}$$

with the exception that

$$\frac{\left|\Delta\omega^{\mathrm{II}}_{\max,\min}\right|}{\left|\Delta\omega^{\mathrm{I}}_{\max,\min}\right|} = \sqrt{\frac{\left|a^{\mathrm{II}}_{1,3}\right|\left|a^{\mathrm{I}}_{3,1}\right|}{\left|a^{\mathrm{I}}_{1,3}\right|\left|a^{\mathrm{I}}_{4,2}\right|}\left[1 + \frac{\left|a^{\mathrm{I}}_{1,3}\right|}{\left|a^{\mathrm{I}}_{2,4}\right|} - \frac{2\left|\Delta\delta_{\mathrm{SEP}}\right|}{\left|a^{\mathrm{I}}_{1,3}\right|t^2_{\mathrm{clr}}}\right]} \tag{11}$$

if the rotor angle has passed its post-fault SEP value at fault clearance. The stage accelerations without cycle identifications in the right side of (9) and (10) are those between the two compared extrema.

We can deduce from (2)–(5) and (9)–(11) that the transient stability of the SMIB system, including the first and second swing stabilities in the first cycle and the aperiodic and oscillatory stabilities in the following cycles, can be uniformly improved by decreasing the magnitudes of the rotor accelerations in stages 1 and 3 and increasing the magnitudes of the rotor accelerations in stages 2 and 4 as much as possible.

2.2. Qualitative Analysis of the Destruction of Stage Sequence due to Improper Control Actions

The relationships obtained above are implicitly assumed to be a natural sequence, i.e., 1-2-3-4-1-2 . . . , where each stage follows the same previous stage in their natural order. However, this natural sequence can be destroyed by improper controller actions, and significantly affecting power system transient stability.

Figure 3 sketches the segments of the electric power versus rotor angle P_e-δ relationship of a synchronous machine in a SMIB system that has been distorted by control actions. The blue segments show a natural stage sequence in one cycle where the stage cycle is 2-3-4-1. The red segments illustrate two cases of the destruction of the natural sequence, which will be analyzed below.
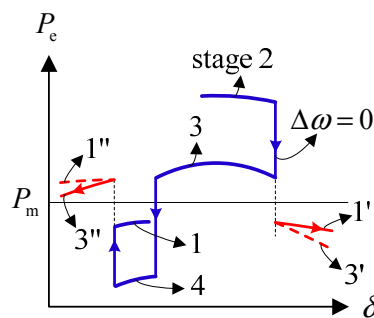

Figure 3. Schematic diagram of the destruction of the stage sequence.

2.2.1. Destruction at Transition from Stage 2 to Stage 3

For a natural transition shown by the blue segments in the right part of Figure 3, the control action in stage 3 should continue decelerating the synchronous generator. Such an action would lead to a negative speed deviation that decreases the accumulated positive angle deviation, but should use a smaller rotor acceleration to reduce the speed deviation that accompanies the process, as illustrated in Figure 2. However, an excessive control action in stage 3, shown by the red segment 3′ in Figure 3, will accelerate the synchronous machine, quickly resulting in a positive speed deviation. The system thus enters into stage 1 after a negligible stay in stage 3; the natural evolution sequence is destroyed and the rotor angle continues to increase. It is very likely that the rotor angle will increase beyond the unstable equivalent point (UEP) and causing an aperiodic instability for the following two reasons. First, the intrinsic P_e-δ characteristic (sine function) tends to reduce the electric power under these circumstances, resulting in a longer stay in stage 1 and a larger consequent angle deviation (i.e., moving further right in the P_e-δ plane). Secondly, the distance to the right UEP is already quite short at the end of stage 2.

2.2.2. Destruction at Transition from Stage 4 to Stage 1

A similar destruction can occur at the transition from stage 4 to stage 1 if the control action in stage 1 is excessive. The system will evolve back to stage 3 from stage 4 after a negligible stay in stage 1, as illustrated by the red segments 1″ and 3″ in the left part of Figure 3. The consequence, however, is much less severe. The angle deviation becomes larger (i.e., moving further left in the P_e-δ plane), but an instability is not likely to happen for the following two reasons. First, the intrinsic P_e-δ characteristic tends to reduce the electric power under such circumstances, thus counteracting the control action in stage 3 and tending to pull the system back to the natural stage sequence. Secondly, the distance to the left UEP at the end of stage 4 is quite far.

The destructions above are both caused by an excessive control action in stage 1 or stage 3. Therefore, these destructions can be avoided by designing more moderate control actions for these two stages.

2.3. Mechanism of Transient Stability Improvement in a SMIB System

After combining the analyses in Sections 2.1 and 2.2, we can hypothesize that the power system transient stability of a SMIB system—including the first and second swing stabilities in the first cycle and the aperiodic and oscillatory stabilities in the following cycles—can be uniformly improved by dramatically increasing the magnitudes of the rotor accelerations in stages 2 and 4 and by moderately decreasing the magnitudes of the rotor accelerations in stages 1 and 3.

3. Analysis of the Physical Factors Influencing the Capability of Wind Turbine Active and Reactive Currents to Affect the Swing Dynamics of Synchronous Machines

The physical factor dependencies are analyzed for a system with two synchronous machines and one aggregated wind turbine, shown in Figure 4a, which experiences a three-phase fault cleared by isolation. The synchronous machines are represented by the classic model and the wind turbine is represented by a controllable current source. The resistance and susceptance of the devices in Figure 4a are all neglected. The resulting equivalent circuits during (Figure 4b) and post fault are arranged into concise forms exhibited in Figure 4c,d.

For this system, we use the following simplifications

$$E_{g1} = E_{g2} \triangleq E_g \text{ (constant)} \tag{12}$$

$$X_2^d = X_2^p \triangleq X_2 \text{ (constant)} \tag{13}$$

where the superscript "d" represents "during fault", and the physical meanings of the undeclared variables can be deduced from Figure 4c,d.
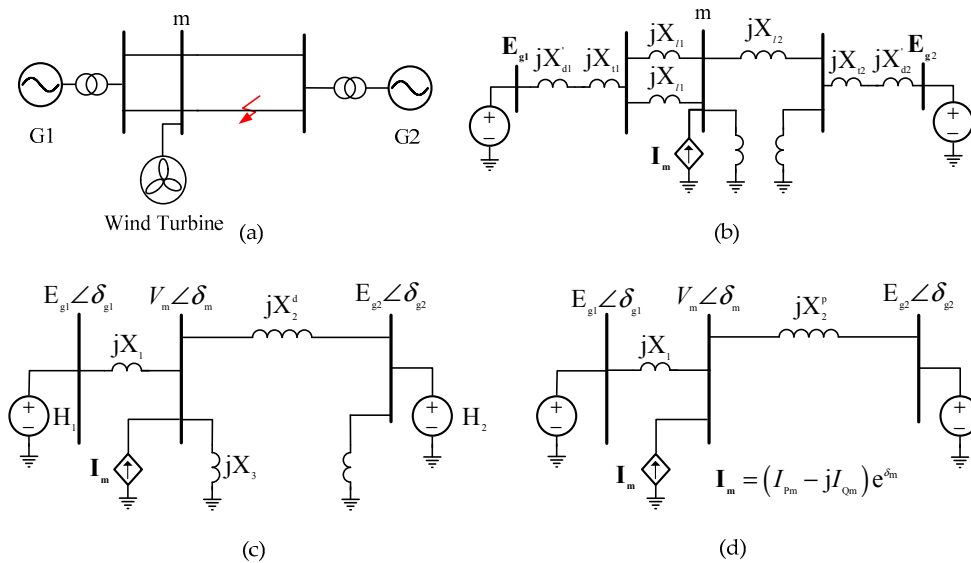

Figure 4. Schematic diagrams: (**a**) a two synchronous machine, one aggregated wind turbine system, (**b**) its equivalent circuit during fault, and (**c**,**d**) the concise equivalent circuits during and post fault, respectively.

3.1. Quantification of the Dependencies

Quantifying precisely how the capability of a wind turbine's active and reactive currents to affect the swing dynamics of synchronous machines is dependent on various physical factors is done in three steps: first quantifying the capabilities, then quantifying the physical factors, and finally determining the dependencies.

First, since rotor acceleration is the intrinsic motivating force of the swing dynamics as discussed in Section 2.1, the capability to affect the swing dynamics can be quantified in terms of the rotor acceleration, given by

$$\Delta a_{12} \triangleq \begin{bmatrix} \Gamma_Q & \Gamma_P \end{bmatrix} \begin{bmatrix} \Delta I_{Qm} & \Delta I_{Pm} \end{bmatrix}^T \tag{14}$$

where Δ here represents a small change, different from those in (1)–(11), a_{12} is the relative rotor acceleration between the two machines in Figure 4 and represents the rotor acceleration of the equivalent SMIB system, and Γ_Q and Γ_P represent the capability of the reactive and active current, respectively, to affect the swing dynamics of the synchronous machines. Furthermore, the magnitudes of Γ_Q and Γ_P reflect the efficiency of optimizing the reactive and active currents, respectively, and their signs in combination with the stage status (i.e., which stage the swing process is in) determine the optimization direction (i.e., to increase or decrease), according to Section 2.3. The resulting expressions of Γ_Q and Γ_P are constructed from the variables in Figure 4c,d.

Secondly, the physical factors are quantified using the variables in Figure 4c,d. The system strength in terms of inertia and link impedance are respectively quantified as

$$H \triangleq H_1 + H_2 \tag{15}$$

$$X \triangleq X_1 + X_2 \tag{16}$$

and the system topology in terms of wind farm location and synchronous-generator (inertia-) distribution are respectively quantified as

$$\alpha \triangleq X_1/(X_1 + X_2) \tag{17}$$

$$\beta \triangleq H_1/(H_1 + H_2) \tag{18}$$

The fault and its location is quantified by

$$\gamma \triangleq X_3/X_2 \tag{19}$$

where an infinite value of γ represents clearance of the fault, and the physical meaning of the undeclared variables in (15)–(19) can be deduced from Figure 4. In addition, the pre-fault power flow and other factors that mainly influence the range of rotor angle δ_{g12} during swings are quantified by the rotor angle δ_{g12}. The physical characteristics of the wind turbines themselves are quantified by their active and reactive current injections I_{Pm} and I_{Qm}.

Third, we substitute the quantified physical factors into the original expressions of Γ_Q and Γ_P, which gives

$$\Gamma_Q = -\frac{E_g \left[(1-\alpha)(1-\beta)\sin(\delta_{g1} - \delta_m) + \alpha\beta\sin(\delta_m - \delta_{g2}) \right]}{2H\beta(1-\beta)(1+\alpha/\gamma)} \tag{20}$$

$$\begin{aligned} \Gamma_P = &\frac{E_g \left[(1-\alpha)(1-\beta)\cos(\delta_{g1} - \delta_m) - \alpha\beta\cos(\delta_m - \delta_{g2}) \right]}{2H\beta(1-\beta)(1+\alpha/\gamma)} + \\ &\frac{\alpha(1-\alpha)E_g \left[(1-\alpha)(1-\beta)\cos(\delta_{g1} - \delta_m) - \alpha\beta\cos(\delta_m - \delta_{g2}) \right](XI_{Qm})}{2H\beta(1-\beta)(1+\alpha/\gamma)\sqrt{E_g^2 \left[1 - 2\alpha(1-\alpha)(1-\cos\delta_{g12}) \right] - [\alpha(1-\alpha)]^2(XI_{Pm})^2}} + \\ &\frac{\alpha(1-\alpha)E_g \left[(1-\alpha)(1-\beta)\sin(\delta_{g1} - \delta_m) + \alpha\beta\sin(\delta_m - \delta_{g2}) \right](XI_{Pm})}{2H\beta(1-\beta)(1+\alpha/\gamma)\sqrt{E_g^2 \left[1 - 2\alpha(1-\alpha)(1-\cos\delta_{g12}) \right] - [\alpha(1-\alpha)]^2(XI_{Pm})^2}} \end{aligned} \tag{21}$$

where

$$\delta_m = \tan^{-1}\frac{(1-\alpha)\sin\delta_{g1} + \alpha\sin\delta_{g2}}{(1-\alpha)\cos\delta_{g1} + \alpha\cos\delta_{g2}} + \sin^{-1}\left[\frac{\alpha(1-\alpha)(XI_{Pm})}{E_g\sqrt{1 - 2\alpha(1-\alpha)(1-\cos\delta_{g12})}} \right] \tag{22}$$

Equations (20) and (21) link the quantified capabilities and the quantified physical factors. Consequently, the dependence of the capabilities on one physical factor can be quantified as the impact of the corresponding variable of this physical factor on the magnitudes and signs of Γ_Q and Γ_P, respectively, given by (20) and (21). In other words, any analysis of the dependencies is changed into an analysis of (20) and (21), which means mathematical tools such as function curves and partial derivatives can now be employed in the analysis.

3.2. Analysis of the Dependencies

This analysis is divided into two parts. The first part provides a general but basic analysis, covering various physical factors. The second part provides an in-depth but specific analysis, focusing on the physical factor of wind turbine active current injection.

3.2.1. A General Basic Analysis

This part will analyze the general differences and similarities between the capability dependencies of a wind turbine's active current and those of the reactive current.

We can deduce from (20) and (21) that the magnitudes of Γ_Q and Γ_P both increase with a decrease in total inertia H, an increase in the inertia-distribution imbalance $|\beta - 0.5|$, or an increase in γ. Furthermore, we can also find that I_{Qm} and I_{Pm} always appear with X in a form of (XI_{Qm}) and (XI_{Pm}), respectively. Combining these deductions with physical meanings of the variables gives the following similarities. Optimizations of the reactive and active current in terms of transient stability improvement are both more effective for inertia-weak grids (i.e., grids with limited synchronous generators) or severely unbalanced synchronous-generator-distribution grids. Additionally, they are both less effective during faults, especially when faults are close to the wind turbine. Besides, a link-weak grid (i.e., a grid with long transmission lines) magnifies both impacts of wind turbine active and reactive currents on the performance of their optimizations.

Figure 5 offers curves of Γ_Q and Γ_P with different parameter values. We can see from Figure 5a,b that the magnitude of Γ_Q decreases as $|\alpha - 0.5|$ increases, while the magnitude of Γ_P, to some extent, increases as $|\alpha - 0.5|$ increases. We can also find that Γ_Q is always heavily affected by the rotor angle δ_{g12}, while Γ_P is barely affected by δ_{g12} when its magnitude is large. Combining these deductions with the physical meanings of the variables shows certain differences. Optimization of the reactive current is more effective when a wind farm is located near the middle of the transmission lines, and is less effective when placed near the ends. In comparison, optimization of the active current is less effective near the middle and more effective near the ends, i.e., complementary to the reactive current. The performance of any reactive current optimization is always heavily affected by any physical factors that heavily influence the rotor angle range during swings, such as pre-fault power flow. In comparison, any effects on active current are negligible when its optimization is considerably effective, e.g., when the wind farm is located at the end of a long transmission line and there are limited synchronous generators nearby (i.e., the wind farm integrates into a weak grid).

The analysis above identifies the general physical factors that may need to be considered during the parameter setting process of the controller. Some of these factors are deterministic, such as the system strength and the wind farm location, and can be handled offline. However, others are not deterministic—or are stochastic like the pre-fault power flow and fault location—and may need online adaptation.
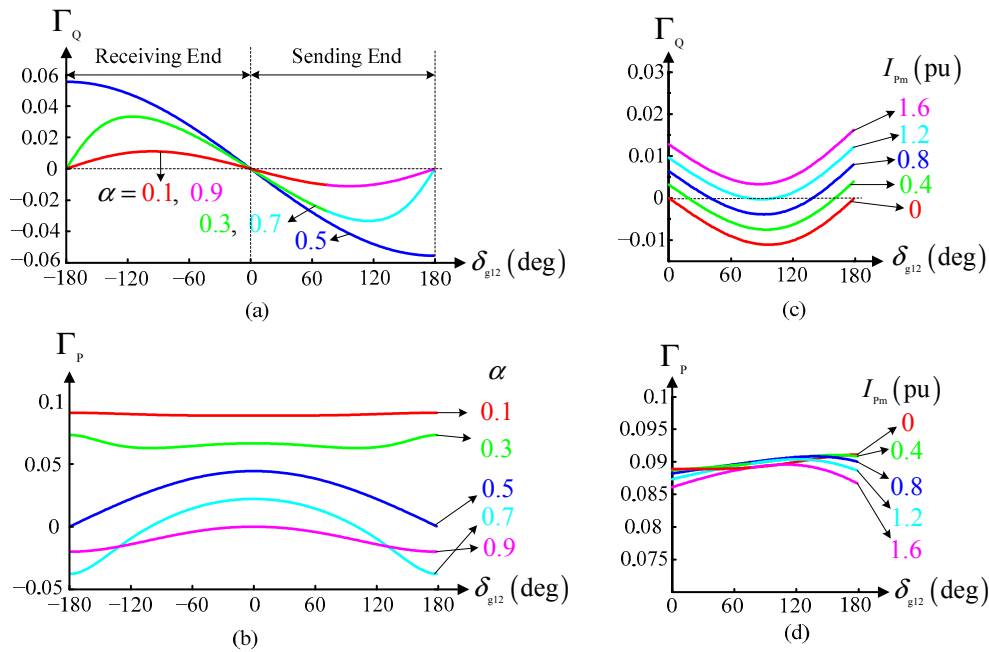
Figure 5. Curves of Γ_Q and Γ_P with different parameter values. The default parameter values are $\gamma = \infty$, $\alpha = \beta = 0.1$, $I_{Pm} = I_{Qm} = 0$, $X = E_g = 1$, and $H = 50$. (**a**) Curves of Γ_Q with different wind farm locations; (**b**) Curves of Γ_P with different wind farm locations; (**c**) Curves of Γ_Q with different levels of wind turbine injecting active current; (**d**) Curves of Γ_P with different levels of wind turbine injecting active current.

3.2.2. An In-Depth Specific Analysis

This section focuses on the physical factor of the active current injection of wind turbines, the most significant difference between wind turbines and power electronic var-compensation devices such as static var compensators (SVCs), which possess many similar characteristics to wind turbines and have been well studied [17,18]. Since the effect of I_{Pm} on Γ_Q and Γ_P, as suggested in (20)–(21), is quite complex and highly dependent on other variables such as α and β, the analysis is restricted to the following condition restrictions: a small α, a small β, a large XI_{Pm}, and a positive δ_{g12}. These conditions represent the scenario for which the proposed controller is designed, i.e., large-scale wind turbines integrate into weak grids.

The curves of Γ_Q and Γ_P under the above conditions and with different active current injection levels (different I_{Pm}) are illustrated in Figure 5c,d. First, the figures illustrate that the magnitude of Γ_P is always much larger than that of Γ_Q, indicating that optimizing the active current is more effective than optimizing the reactive current under the given scenarios. This conclusion agrees with the general analysis in terms of wind farm location described in Section 3.2.1.

Secondly, we can see from Figure 5c,d that the curves of Γ_Q are highly distorted by I_{Pm}, while the distortion for Γ_P is negligible. When I_{Pm} equals zero, as in the case of var-compensation devices, the sign of Γ_Q is completely negative. Combining this result with the analysis in Section 2.3 gives the conclusion that boosting the reactive current during the first swing is beneficial for first swing stability improvement, and that further optimization of reactive current post the first swing for further stability improvement only needs the information of stage status and thus is easy to implement. When I_{Pm} increases to a large non-zero value (technically, XI_{Pm} increases to a large non-zero value, see the similarities in Section 3.2.1), as in the case of wind turbines, the sign of Γ_Q becomes partially negative or completely positive. Combining this with Section 2.3 suggests that the beneficial effects of reactive current boosting are weakened or can even become detrimental, and that a high-efficiency controller of reactive current during or post the first swing now needs extra information concerning the sign of

Γ_Q. However, as shown in Figure 5c, this sign further depends on rotor angle δ_{g12}, a variable hard to estimate both offline and online. Therefore, a large-scale active current injection weakens or even reverses the beneficial impacts of reactive current boosting during the first swing, and makes the implementation of a high-efficiency controller of reactive current extremely difficult.

The high resistance of Γ_P to I_{Pm}, shown in Figure 5d, eliminates the adverse impacts similar to those in the case of Γ_Q. An always positive Γ_P, in combination with the analysis in Section 2.3, suggests that a reduction in active current during the first swing is always beneficial for first swing stability improvement, and that further optimization of active current after the first swing for further stability improvement simply needs the information of stage status, regardless of the active current injection level. Therefore, a high-efficiency active current controller is easier to implement, under the given scenarios, than a similar reactive current controller, since it does not need any extra information that is hard to acquire, such as the rotor angle δ_{g12}.

The above analysis shows the superiority of using active current over reactive current as the control object to improve the transient stability of weak grids with large-scale integrations of wind turbines. That is, the optimization of active current is more effective, and is easier to implement under these situations. Furthermore, the optimization of active current is also more flexible, as reactive current optimization is highly restricted by voltage supporting and regulating requirements.

Note that the same conclusions as those drawn from the qualitative analysis of the function curves of Γ_Q and Γ_P in this section can also be drawn from a strict but lengthy mathematical analysis of the respective partial derivatives of Γ_Q and Γ_P, which have not been presented here for the sake of brevity.

4. Main Structure and Settings Approach for the Proposed Controller

This section presents the main structure for the proposed controller, as well as an approach for determining the most appropriate settings for the controller. The controller is designed to improve the transient stability of weak grids with large-scale wind turbine integration by optimizing the behavior of the wind turbine current.

4.1. Main Structure

The controller optimizes the behavior of a wind turbine's active current, since it is more effective, more flexible, and easier to implement than optimizing the reactive current under the situations for which the controller is designed, according to the analysis conducted in Section 3.2.2. The active current behavior is optimized by superimposing a corrective reference ΔI_P^{ref} on the original reference. The corrective reference is generated in a particular fashion depending on the stage status, i.e.,

$$\Delta I_P^{ref} = \begin{cases} -K_P \times a & \text{stage 1, 3} \\ \Delta I_{Pmin}^{ref} & \text{stage 2} \\ \Delta I_{Pmax}^{ref} & \text{stage 4} \end{cases} \tag{23}$$

The corrections in stages 1 and 3, according to Section 2.3, are moderate, being proportional to the rotor acceleration to avoid destruction of the stage sequence. The corrections in stages 2 and 4, according to Section 2.3, are more dramatic, reaching their minimum or maximum, respectively. All corrections depend on an assumption that Γ_P is always positive under the conditions that the controller is designed for, as determined from the analysis in Section 3.2.2. The rotor acceleration a is that of the system's equivalent SMIB system, and can be estimated by the rotor acceleration of a representative synchronous generator in the critical cluster, or by the relative rotor acceleration of two synchronous generators respectively in the critical and remaining clusters [19]. The extrema of the corrections depend on the applied tolerances of the wind turbine. The proportional gain K_P determines how much active current correction is needed to moderately decrease the magnitude of

rotor acceleration in stages 1 and 3. This gain corresponds to the reciprocal of the quantified capability of the active wind turbine current to affect synchronous machines as described in Section 3.1, given by

$$K_P = \frac{1}{\Gamma_P} \triangleq K_{PD} K_{PS} \tag{24}$$

where K_{PD} handles the deterministic influential physical factors, such as the system strength, and K_{PS} handles the stochastic factors such as the pre-fault power flow. These physical factors were identified in Section 3.2.1.

The actions of the proposed controller in different stages are sketched in Figure 6.
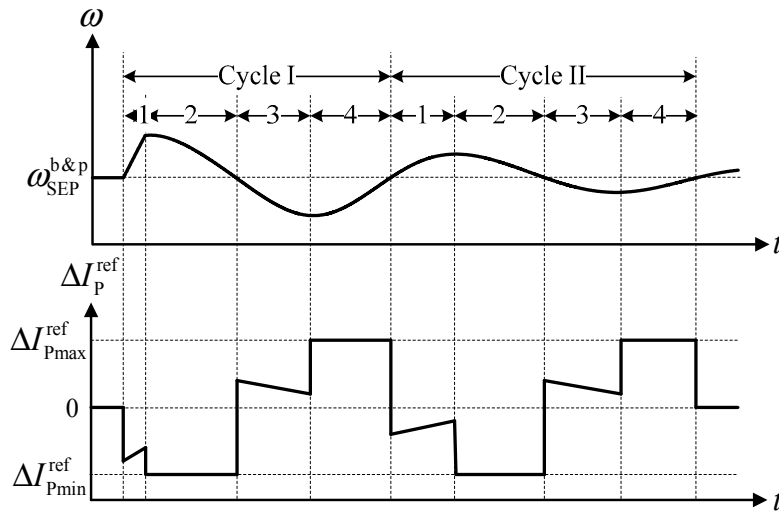

Figure 6. Schematic diagram of the control actions of the proposed controller in different stages.

4.2. Settings Optimization

The method for optimizing the settings is as follows. First, define a fault set. Next, the equivalent circuits of the system during and post fault in the fault set should be equaled or simplified to forms as in Figure 3c,d, and the determined parameters should be calculated.

Secondly, calculate K_{PD} according to

$$K_{PD} = \frac{1}{\Gamma_{PD}} \tag{25}$$

where Γ_{PD} represents Γ_P when the stochastic parameters are given the values

$$\gamma = \infty; \ X_2 = \overline{X_2^p}; \ I_{Qm} = I_{Pm} = 0; \ \delta_{g12} = 90^\circ \tag{26}$$

where $\overline{X_2^p}$ is the mean value of X_2^p for the faults in the defined fault set.

Third, calculate K_{PS} to correct the errors caused by deviations in the stochastic parameters from those in (26). Only the stochastic physical factor of fault location is considered, since the effects of other stochastic physical factors on Γ_P are negligible, as discussed in Section 3.2. The fault location is estimated online by the terminal voltage dip of the wind turbine, and their relationship is estimated offline for the fault set defined. Eventually, we arrive at

$$K_{PS} = f(V_m) = \begin{cases} k \cdot V_m + b & V_m \le 0.9 \\ 1 & V_m > 0.9 \end{cases} \tag{27}$$

5. Applying the Proposed Controller and Its Settings Optimization to Kundur's Two-Area System Modified with Wind Turbine Integration

An application of the proposed controller and the method for determining its settings to a test system is provided in this section. There are many common test systems for power system transient stability study such as WSCC 9-bus system, Kundur's two-area system, New England system and Nordic32 system. We chose Kundur's two-area system [20], since it is a typical weak grid featured with long transmission lines and heave power flows. This test system was modified by replacing G2 with an equivalent wind farm (467×1.5 MW/1.67 MVA). The modification further weakened the strength of the system by reducing the inertia of the system. The wind farm was represented by an aggregated wind turbine. The pre-fault active power of G2 was balanced by the wind farm, and the reactive power was balanced by a STATCOM. Additionally, the transmission lines between bus 5–6, 6–7, 9–10 and 10–11 were doubled in both number and length (i.e., technically no change). The modified two-area system is shown in Figure 7, and the information about the system strength and pre-fault power flow is provided in Table 1. Figure 7 also illustrates the measurement point of the corridor power in Table 1 and the default fault location.
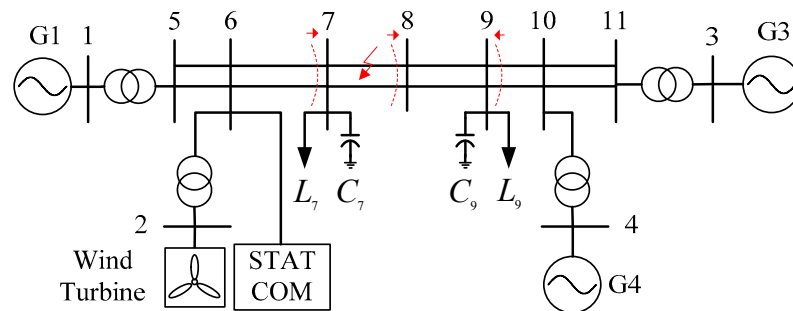

Figure 7. Schematic diagram of modified Kundur's two-area system.

Table 1. Information of modified Kundur's two-area system.

System Strength		System Power Flow		
Length of Lines	Inertia of SGs	Wind Turbine	SGs	Corridor Power
5–6, 10–11: 50 km	G1: 6.5 pu	Total capacity: 780 MVA	G1: 700 MW	Bus 7: 1370 MW
6–7, 9–10: 20 km	G3: 6.175 pu	Total power: 700 MW	G3: 766 MW	Bus 8: 361 MW
7–8, 8–9: 110 km	G4: 6.175 pu	Wind speed: 11.5 m/s	G4: 700 MW	Bus 9: 1429 MW

The model of the aggregated wind turbine was based on [21]. The original supplementary controllers of current references preferentially boosted the reactive current and depressed the active current based on voltage dip. The structure of the original controllers, as well as their parameter settings, are presented in Figure 8, which also demonstrates a way to incorporate the proposed controller. The models and parameter settings of other elements in the system are the same as those in [20]. The fourth excitation control system in [20] was used for the synchronous generators, i.e., a thyristor exciter with high gain and power system stabilizer.
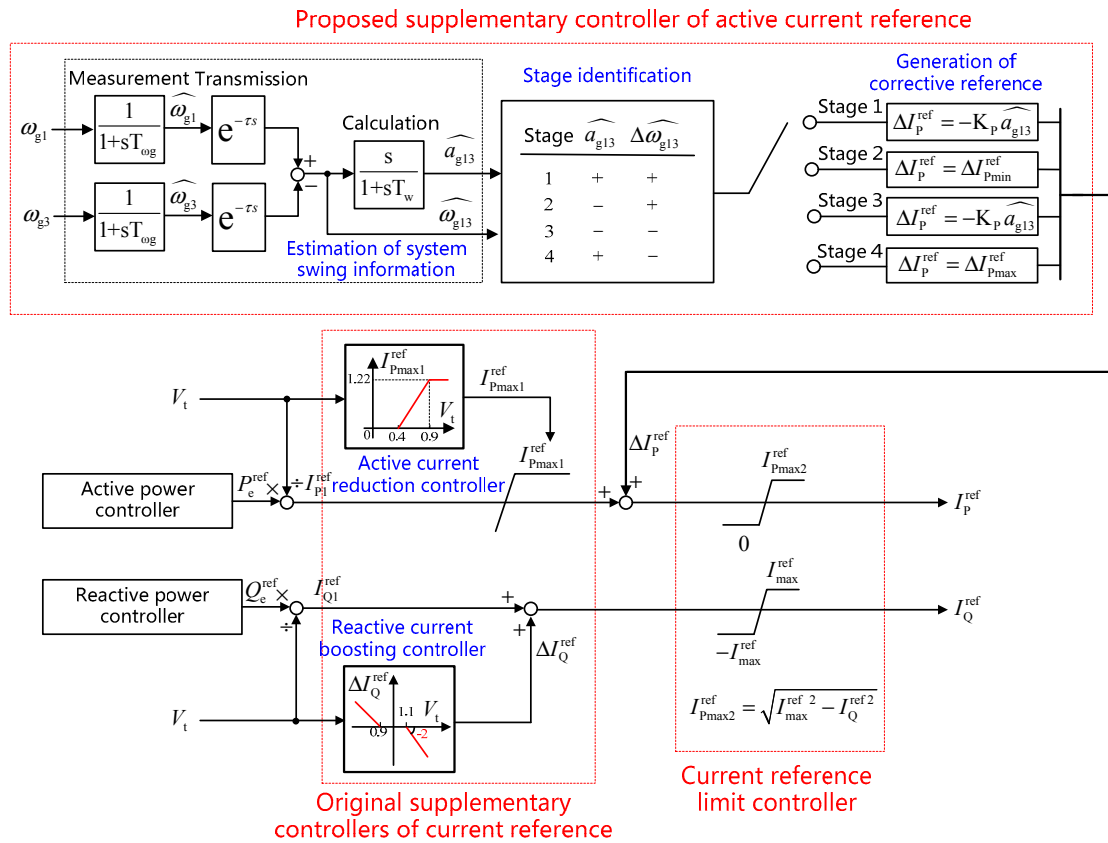
Figure 8. Schematic diagram of parts of the aggregated wind turbine model with the proposed controller.

For the parameter setting process of the proposed controller, we neglected the resistance and susceptance of the devices in Figure 7, and all shunt-connected devices (excluding the wind turbines) along the transmission lines such as loads and capacitors. The fault set was chosen to be three-phase short-circuit faults on transmission line segments 7–8 and 8–9. The setting results are

$$K_{PD} = 21; \ k = -1.78; \ b = 2.60; \ \Delta I^{ref}_{Pmax} = 0 \ \text{pu}; \ \Delta I^{ref}_{Pmin} = -1 \ \text{pu} \tag{28}$$

In the simulation, the rotor acceleration/speed of the system's equivalent SMIB system was estimated by the relative rotor acceleration/speed between G1 and G3, shown in Figure 8. The resulting parameter settings are

$$T_{\omega g} = 30 \ \text{ms}; \ \tau = 30 \ \text{ms}; \ T_w = 5 \ \text{ms} \tag{29}$$

where the time constant of the frequency measurement setting $T_{\omega g}$ is based on [22], and the transmission delay setting τ is from [23].

The action of the proposed controller was limited to the first two cycles to avoid an increasingly detrimental effect of the delays of Figure 8 in subsequent cycles. This is because the durations of the stages—particularly stages 2 and 4 as illustrated in Figure 2—decrease with the damping of the swings, which increases the relative error in stage status caused by the delays and further deteriorates the efficiency of the controller.

The performance of the proposed controller and its settings optimization method were evaluated in three aspects, namely fault location, wind speed, and system strength. Multiple case pairs were designed for each aspect, and the only difference within each case pair was whether the proposed controller was incorporated into the wind turbine control or not. The resulting power system transient stability levels were assessed according to the critical clearing time (CCT), with a standard error of

10 ms. The CCT was determined by multiple time-domain simulations. The performance of the proposed controller under each case pair was thus quantified as the improvement in CCTs.

The proposed controller was first evaluated under different fault locations. Six case pairs were designed, representing a fault location at the middle of the transmission line segment 5–6, 6–7, 7–8, 8–9, 9–10, and 10–11, respectively. The fault was a three-phase short-circuit fault and was cleared by isolating the faulted line segment. Table 2 shows the CCT results. The improvements (imp.) of the CCTs with (w/) the proposed controller, compared to those without (w/o) the proposed controller, suggest a high performance of the proposed controller under different fault locations.

Table 2. CCT (ms) results under different fault locations.

| | Fault Location, at 50% of Line | | | | | |
	5–6 [a]	6–7	7–8	8–9	9–10	10–11
w/	170	80	320	670	600	580
w/o	250	230	630	1720	1360	870
imp.	47%	188%	97%	157%	127%	50%

[a]: The type of active power load was changed from the original constant current type into a constant impedance type to avoid a non-convergence result in the simulation.

The proposed controller was then evaluated under different wind speeds. Apart from the default wind speed of 11.5 m/s, four more wind speeds were considered as shown in Table 3, which also exhibits the pre-fault active power output, rotor speed and pitch angle of the wind turbine under these wind speeds. The possible change in wind turbine active power output caused by the different wind speed was balanced by adjusting the active power outputs of the synchronous generators in proportion to their capacities. Therefore, the pre-fault power flow of the system might also be changed. Table 3 presents the pre-fault corridor power flow near bus 8 under these wind speeds. For each case pair, the fault was located at the middle of the line segment 7–8, and the type and clearance of the fault as well as other settings were the same as above. Table 4 presents the results. The improvements in CCTs verify the efficiency of the controller under different wind speeds.

Table 3. System information under different wind speeds.

| | Wind Speed (m/s) | | | | |
	14.2	11.5	10.1	8.7	6.9
Wind turbine active power (pu)	1.0	1.0	0.75	0.5	0.25
Wind turbine rotor speed (pu)	1.2	1.2	1.2	1.19	0.95
Wind turbine pitch angle (degree)	10	0	0	0	0
Corridor power near bus 8 (MW)	361	361	249	132	15

Table 4. CCT (ms) results under different wind speeds.

| | Wind Speed (m/s) | | | | |
	14.2	11.5	10.1	8.7	6.9
w/	320	320	440	510	600
w/o	630	630	740	890	900
imp.	97%	97%	68%	75%	50%

Finally, the proposed controller was evaluated under different grid strengths. The strength of the test system in terms of link impedance was changed by proportionally adjusting the lengths of all transmission lines to 75% or 125% of their original values. The strength in terms of inertia was changed by proportionally adjusting the inertias of all synchronous generators to 75% or 125%.

The parameter settings of the proposed controller were re-calculated, since some of the influential parameters recognized in Section 3.2.1 had been changed. Table 5 shows the controller settings and the short-circuit ratios (SCRs) at bus 2 (i.e., the SCR for the wind farm) under these grid strengths. The fault sequence and other settings remained unchanged. Table 6 presents the CCT results. As can be found from Table 6, the improvements in CCTs increase with the decrease of the system strength. In other words, the proposed controller performs better under weak grids. This finding conforms to the analysis of Section 3.2.1, which states that the performance of active current optimization would be better under weak grids.

Table 5. System information under different grid strengths.

	Length of Lines (pu)			Inertia of SGs (pu)		
	75%	**100%**	**125% [b]**	**75%**	**100%**	**125%**
SCR at bus 2	2.34	2.11	1.92	2.11	2.11	2.11
K_{PD}	23	21	20	16	21	26
k of $f(V_m)$	−1.73	−1.78	−1.80	−1.78	−1.78	−1.78
b of $f(V_m)$	2.55	2.60	2.62	2.60	2.60	2.60

[b]: The active power of G1 as well as those of L7 and L9 are simultaneously decreased by 100 MW, so that a post-fault SEP would exist.

Table 6. CCT (ms) results under different grid strengths.

	Length of Lines (pu)			Inertia of SGs (pu)		
	75%	**100%**	**125% [b]**	**75%**	**100%**	**125%**
w/	690	320	410	270	320	350
w/o	920	630	770	650	630	700
imp.	33%	97%	88%	141%	97%	100%

[b]: The active power of G1 as well as those of L7 and L9 are simultaneously decreased by 100 MW, so that a post-fault SEP would exist.

Time-domain dynamics of some variables within the case pair corresponding to 125% length of all transmission lines are provided in Figure 9, with a fault duration of 410 ms. Figure 9a shows the dynamics of the variables that reflect the action of the proposed controller. The mismatch between the corrective reference ΔI_P^{ref} and the final reference I_P^{ref} during fault was due to the action of the current reference limit controller shown in Figure 8. The 300 $\omega_{g13}^{\hat{}}$ means 300 times of the $\omega_{g13}^{\hat{}}$. Figure 9b exhibits the active power, reactive power and terminal voltage of the aggregated wind turbine. The impact of the proposed controller on the rotor speed of the wind turbine is illustrated in Figure 9c, which also presents the dynamics of other related variables including the pitch angle and the mechanical and electrical torques. The mismatch between the electric torque in Figure 9c and the electric power in Figure 9b was due to the action of the dynamic braking resistor that activates when the output power is much less than its order and causes an unacceptable DC-link voltage increase. The impacts on the synchronous generators are provided in Figure 9d–f, demonstrating dynamics of active power outputs, rotor speeds, and relative rotor angles of/among synchronous generators, respectively.
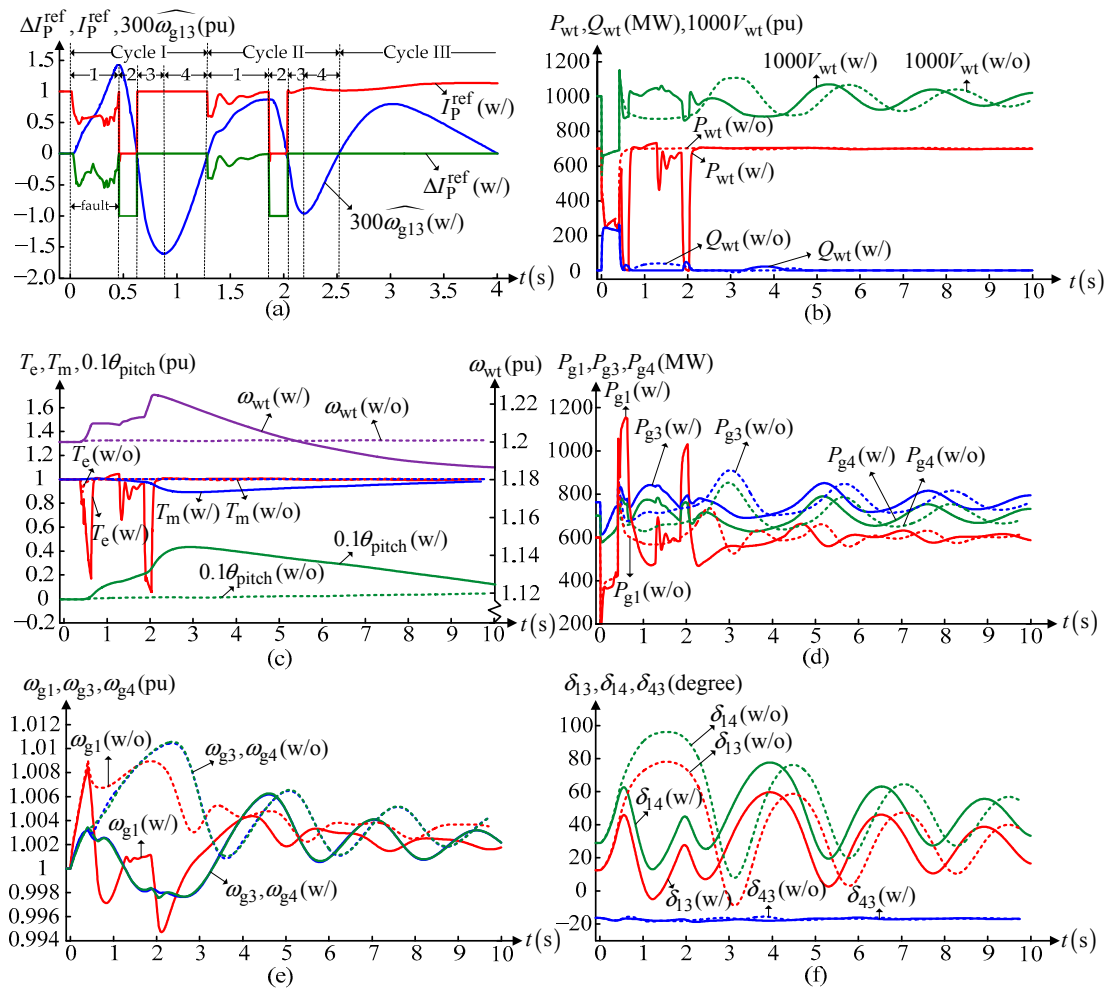
Figure 9. Time-domain dynamics of some variables within the case pair corresponding to 125% length of all transmission lines with 410 ms fault duration. (**a**) Dynamics of the corrective reference of the proposed controller, the final active current reference of the wind turbine and the estimated relative rotor speed between G1 and G3; (**b**) Dynamics of wind turbine active power, reactive power and terminal voltage; (**c**) Dynamics of electric torque, mechanical torque and pitch angle of the wind turbine; (**d**) Dynamics of active power of synchronous generators G1, G3, and G4; (**e**) Dynamics of rotor speeds of synchronous generators G1, G3, and G4; (**f**) Dynamics of relative rotor angles among synchronous generators G1, G3, and G4.

6. Conclusions

This paper addressed the issue of transient stability of weak grids with large-scale wind turbine integration by optimizing the active current behavior of wind turbines based on analyses of two associated problems. First, an analysis of the mechanism underlying transient stability improvement within a SMIB system concluded that the transient stability of a SMIB system—including the first and second swing stabilities and other aperiodic or oscillatory stabilities—can be uniformly improved by dramatically increasing the magnitude of rotor acceleration in stages 2 and 4 and by moderately decreasing the magnitude in stages 1 and 3. Secondly, an analysis of the physical factor dependencies determining how a wind turbine's active and reactive currents affect the swing dynamics of synchronous machines found that reactive and active currents are both more effective for inertia-weak grids, and are complementary in terms of wind farm location. The analysis also found that compared to reactive current, active current optimization is more effective, more flexible,

and easier to implement for improving the transient stability of weak grids with large-scale wind turbine integration.

This paper proposed an active current reference controller for wind turbines to improve the transient stability of weak grids with large-scale wind turbine integration that included a parameter setting approach. Both methods were based on analyses of the two associated problems. Case studies using a Kundur two-area system, a typically weak grid, verified the efficiency of the controller and validated the analyses.

Author Contributions: Dongliang Zhang and Xiaoming Yuan propose the main idea of the paper; Dongliang Zhang also implements the mathematical and simulation analyses. The paper is written by Dongliang Zhang and is revised by Xiaoming Yuan.

Conflicts of Interest: The authors declare no conflict of interest.

References

1.　Li, J.; Cai, F.; Qiao, L.; Xie, H.; Gao, H.; Yang, X.; Tang, W.; Wang, W.; Li, X. China Wind Energy Outlook 2012. Available online: http://www.gwec.net/wp-content/uploads/2012/11/China-Outlook-2012-EN.pdf (accessed on 18 September 2012).
2.　Vittal, E.; O'Malley, M.; Keane, A. Rotor angle stability with high penetrations of wind power. *IEEE Trans. Power Syst.* **2012**, *27*, 353–362. [CrossRef]
3.　Liu, Z.; Liu, C.; Li, G.; Liu, Y.; Liu, Y. Impact study of PMSG-based wind power penetration on power system transient stability using EEAC theory. *Energies* **2015**, *8*, 13419–13441. [CrossRef]
4.　Elias, J.; Jose, F. Critical clearing time and wind power in small isolated power systems considering inertia emulation. *Energies* **2015**, *8*, 12669–12684.
5.　Ying, J.; Yuan, X.; Hu, J. Inertia characteristic of DFIG-based WT under transient control and its impact on the first-swing stability of SGs. *IEEE Trans. Energy Convers.* **2017**, *PP*, 1. [CrossRef]
6.　Gautam, D.; Vittal, V.; Harbour, T. Impact of increased penetration of DFIG-based wind turbine generator on transient and small signal stability of power systems. *IEEE Trans. Power Syst.* **2009**, *24*, 1426–1434. [CrossRef]
7.　Wang, Z.; Shen, C.; Liu, F. Probabilistic analysis of small signal stability for power systems with high penetration of wind generation. *IEEE Trans. Energy Convers.* **2016**, *7*, 1182–1193. [CrossRef]
8.　Doherty, R.; Mullane, A.; Nolan, G.; Burke, D.; Bryson, A.; O'Malley, M. An assessment of the impact of wind generation on system frequency control. *IEEE Trans. Power Syst.* **2010**, *25*, 452–460. [CrossRef]
9.　Liu, Y.; Jiang, L.; Wu, Q.; Zhou, X. Frequency control of DFIG-based wind power penetrated power systems using switching angle controller and AGC. *IEEE Trans. Power Syst.* **2016**, *32*, 1553–1567. [CrossRef]
10.　He, W.; Yuan, X.; Hu, J. Inertia provision and estimation of PLL-based DFIG wind turbines. *IEEE Trans. Power Syst.* **2017**, *32*, 510–521. [CrossRef]
11.　Ullah, N.R.; Thiringer, T.; Karlsson, D. Voltage and transient stability support by wind farms complying with the E.ON Netz grid code. *IEEE Trans. Power Syst.* **2007**, *22*, 1647–1656. [CrossRef]
12.　Weise, B. Impact of K-factor and active current reduction during fault-ride-through of generating units connected via voltage-sourced converters on power system stability. *IET Renew. Power Gener.* **2015**, *9*, 25–36. [CrossRef]
13.　Shewarega, F.; Erlich, I.; Rueda, J. Impact of large offshore wind farms on power system transient stability. In Proceedings of the IEEE Power Systems Conference and Exposition, Seattle, WA, USA, 15–18 March 2009; pp. 1–8.
14.　Mitra, A.; Chatterjee, D. Active power control of DFIG-based wind farm for improvement of transient stability of power systems. *IEEE Trans. Power Syst.* **2016**, *31*, 82–93. [CrossRef]
15.　Yu, M.; Dysko, A.; Roscoe, A.; Booth, C.; Ierna, R.; Urdal, H.; Zhu, J. Effects of swing equation-based inertial response (SEBIR) control on penetration limits of non-synchronous generation in the GB power system. In Proceedings of the International Conference on Renewable Power Generation, Beijing, China, 17–18 October 2015; pp. 1–6.

16. Alipoor, J.; Miura, Y.; Ise, T. Power system stabilization using virtual synchronous generator with alternating moment of inertia. *IEEE J. Emerg. Sel. Top. Power Electron.* **2015**, *3*, 451–458. [CrossRef]
17. Ledwich, G.; Jordan, T. Placement of shunt VAR systems. *Electr. Power Syst. Res.* **1982**, *5*, 299–306. [CrossRef]
18. Tan, Y.; Wang, Y. Effects of FACTS controller line compensation on power system stability. *IEEE Power Eng. Rev.* **1998**, *18*, 55–56. [CrossRef]
19. Xue, Y.; Custem, T.; Pavella, M. Extended equal area criterion justifications, generalizations, applications. *IEEE Trans. Power Syst.* **1989**, *4*, 44–52. [CrossRef]
20. Kundur, P. *Power System Stability and Control*; McGraw-Hill: New York, NY, USA, 1994.
21. Pourbeik, P.; Sanchez-Gasca, J.; Senthil, J.; Weber, J.; Zadehkhost, P.; Kazachkov, Y.; Tacke, S.; Wen, J.; Ellis, A. Generic dynamic models for modelling wind power plants and other renewable technologies in large scale power system studies. *IEEE Trans. Energy Convers.* **2016**, *PP*, 1. [CrossRef]
22. Bifaretti, S.; Lidozzi, A.; Solero, L.; Crescimbini, F. Anti-islanding detector based on a robust PLL. *IEEE Trans. Ind. Appl.* **2015**, *51*, 398–405. [CrossRef]
23. Gajrani, K.; Sharma, K.; Bhargava, A. Performance assessment of communication network in WAMS. *Int. J. Distrib. Parallel Syst.* **2012**, *3*, 127–137. [CrossRef]